European Journal of Mechanics B/Fluids 28 (2009) 660–669

Contents lists available at ScienceDirect

European Journal of Mechanics B/Fluids

journal homepage: www.elsevier.com/locate/ejmflu

Fast numerical evaluation of flow fields with vortex cells

T. Hetsch [a,*], R. Savelsberg [b], S.I. Chernyshenko [c], I.P. Castro [b]

[a] Aircraft Research Association Ltd, Manton Lane, Bedford, MK41 7PF, UK
[b] School of Engineering Sciences, University of Southampton, Highfield, Southampton, SO17 1BJ, UK
[c] Department of Aeronautics, Imperial College London, London SW7 2AZ, UK

ARTICLE INFO

Article history:
Received 3 November 2008
Received in revised form
2 March 2009
Accepted 6 May 2009
Available online 24 May 2009

Keywords:
Vortex cells
Separation control
Cyclic boundary layers
Cavity flow

ABSTRACT

A vortex cell (in this paper) is an aerodynamically shaped cavity in the surface of a body, for example a wing, designed specially to trap the separated vortex within it, thus preventing large-scale unsteady vortex shedding from the wing. Vortex stabilisation can be achieved either by the special geometry, as has already been done experimentally, or by a system of active control. In realistic conditions the boundary and mixing layers in the vortex cell are always turbulent. In the present study a model for calculating the flow in a vortex cell was obtained by replacing the laminar viscosity with the turbulent viscosity in the known high-Reynolds-number asymptotic theory of steady laminar flows in vortex cells. The model was implemented numerically and was shown to be faster than solving the Reynolds-averaged Navier–Stokes equations. An experimental facility with a vortex cell was built and experiments performed. Comparisons of the experimental results with the predictions of the model are reasonably satisfactory. The results also indicate that at least for flows in near-circular vortex cells it is sufficient to have accurate turbulence models only in thin viscous layers, while outside the viscosity should only be small enough to make the flow effectively inviscid.

1. Introduction

As a rule, flows past bluff bodies are unsteady at sufficiently high Reynolds numbers. Vortices formed by separation are shed downstream in a regular periodic or irregular chaotic process. Generating a wake having high kinetic energy leads to the large drag observed in separated flows. If the process of vortex shedding were prevented the drag would be reduced: this is the idea of a trapped vortex. A vortex cell is a cavity in the body surface designed to accommodate a trapped vortex. The pioneering paper by Ringleb [1] played an important role in dissemination of these ideas, even though some of the formulae in it did not take into account the Routh rule [2]. As a result, some of Ringleb's results on trapped vortices were incorrect [3].

On observing a particularly high-lift under a certain condition during a glider flight, W.A. Kasper suggested (and patented the idea, see [4]) that it was due to a trapped vortex. This observation was not confirmed by wind-tunnel tests, however [5]. Wu and Wu [6] hypothesised that in the flight test the vortex was stabilised by wing vibrations, while in the wind-tunnel experiment the model was rigid. Indeed, at least within a point-vortex model, stabilisation can be achieved by introducing suitable oscillations into the flow [7]. In the late eighties-early nineties an aircraft, EKIP [8], was designed, patented [9], built, and flight-tested in Russia. EKIP was equipped with four vortex cells trapping vortices in the rear part of its body. However, no information on the EKIP vortex cell performance has been published in peer-reviewed journals.[1] While the evidence from the Kasper wing and EKIP remains inconclusive, it is clear that the viability of the trapped vortex concept depends on the vortex stability, so it could possibly be improved by advances in active flow control techniques.

In high-Reynolds-number flows unsteadiness is due not only to the large-scale vortex shedding but also to the turbulence in the boundary and mixing layers. Naturally, full control of turbulence is rather difficult to achieve. Wu and Wu [6] pointed out that, fortunately, drag reduction can be achieved by preventing only the large-scale vortex shedding rather than fully suppressing the turbulence.

There are geometries for which large-scale vortex shedding from the separation eddy does not occur, as in [10–12]. In these

[1] In addition to the references given above our sources of information on EKIP are the seminar presentations on EKIP at the Moscow University, given by EKIP designer Prof. L. N. Schukin, which one of the authors (SC) attended, and an account of our colleague, Prof. G.Yu. Stepanov, who went to the Saratov Aviation Plant and inspected the aircraft.

* Corresponding author. Tel.: +44 1234321680; fax: +44 1234328584.
E-mail address: thetsch@ara.co.uk (T. Hetsch).

0997-7546/$ – see front matter © 2009 Published by Elsevier Masson SAS.
doi:10.1016/j.euromechflu.2009.05.003

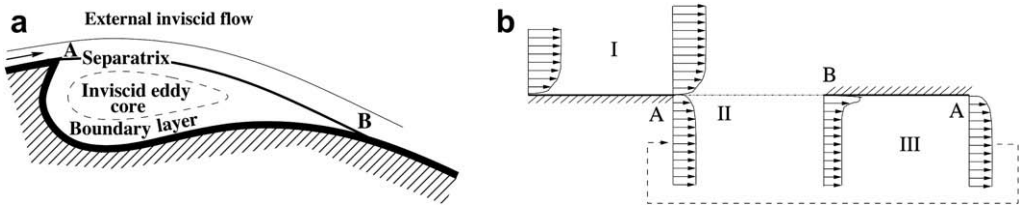

Fig. 1. a). Schematic sketch of a general vortex cell; b). Realisation of this model in the cyclic boundary layer code.

cases, however, the dividing streamline can be replaced with a wall along which the pressure gradient is favourable and, therefore, the vortex cell is not actually needed. A trapped vortex can be stabilised by constant suction [9,13], but more complicated forms of control should be more energy-efficient. In various contexts an open-loop control of trapped vortices was considered in [7] and [14]. A comprehensive review of open and closed-loop control techniques is given in [15], while the recent work by Pastoor et al. [16] demonstrates the advantage of stabilisation of large-scale vortex shedding by closed-loop control.

We will assume now that the flow with a trapped vortex is stabilised and consider the way the stabilised flow can be calculated. The majority of the theoretical work on flows with trapped vortices has been done using the point-vortex, or Föppl, model. Rather than giving an overview of this substantial body of work, we cite only the latest paper [17] where further references can be found. While it is simple, the point-vortex model has severe limitations. There are geometries for which a steady point-vortex flow cannot satisfy the Kutta–Joukowski condition. This is unphysical and is caused by the imperfection of the model, because the steady solution of the Navier–Stokes equation always exists [18], at least in closed domains, and at high Reynolds numbers, of course, it satisfies the Kutta–Joukowski condition.

In those cases when the Kutta–Joukowski condition can be satisfied in a point-vortex flow it is usually used to determine the circulation of the point-vortex, otherwise the solution is not unique. This method of eliminating non-uniqueness also contradicts the physical mechanisms governing such flows. In fact, an inviscid flow with closed streamlines can have an almost arbitrary distribution of vorticity across the streamlines, $\omega = \omega(\psi)$, and it also can have a velocity discontinuity corresponding to a jump B in the Bernoulli constant across the dividing streamline (that is the streamline separating the closed streamline region from the rest of the flow domain, marked 'Separatrix' in Fig. 1(a)). In contrast, viscous flows are either unique or have a finite number of solutions. Since an inviscid flow is an approximation of a viscous flow with very small viscosity or, more precisely, with a large Reynolds number, rather than assuming $B = 0$ and concentrating all the vorticity in a point, as is done by the point-vortex method, the correct way of eliminating the non-uniqueness of the inviscid flow is to select that inviscid flow which is the limit of the viscous flow as the viscosity tends to zero. For (steady) laminar flows this approach leads to the famous Prandtl-Batchelor theorem [19] and the Batchelor model [20].[2] The Batchelor model, proposed initially for describing the high-Reynolds-number asymptotics of the flow past a bluff body (see the review [21]), is actually more appropriate for flows with trapped vortices (see [22] for the full description of the laminar high-Reynolds-number solution and further references). The most important physical mechanism revealed by high-Reynolds-number asymptotic studies is the balance between acceleration and deceleration of fluid particles along the closed streamline by viscous forces. Since it is a balance between two effects proportional to viscosity, it remains satisfied however small viscosity is. For the case of a constant viscosity coefficient this leads to the Prandtl-Batchelor theorem, stating that in the high-Reynolds-number limit the vorticity inside the eddy is constant, $\omega(\psi) = \text{const}$. When applied to a boundary layer surrounding the eddy this balance also gives an extra condition which, together with the Kutta–Joukowski condition, allows determination of both ω and B. Further details can be found in the papers cited above.

High-Reynolds-number asymptotic studies of flows with trapped vortices [22] also revealed that the trapped vortex should be accommodated in a vortex cell that is a specially designed cavity in the airfoil surface. Otherwise, the flow in the recirculating eddy separates again, creating another region of closed streamlines. The secondary separation gives a flow of a more complicated topology having more inflection points in the velocity profiles. Not only is such a flow more difficult to stabilise but, even if it is stabilised, it would have large velocity gradients, a higher rate of energy dissipation and, hence, higher drag. Numerical optimisation of the vortex cell shape will require a large number of vortex cell flow calculations which, therefore, have to be fast. The present paper describes a step towards developing a fast method of calculating flows with vortex cells.

2. Approximate model of the flow with a vortex cell

It is worth repeating that while there will be no large-scale vortex shedding in the stabilised flow with a vortex cell, the flow will remain turbulent in realistic conditions. An approximate model for the mean turbulent flow used in the present study is obtained by adjusting the laminar high-Reynolds-number theory of flows with trapped vortices, as suggested in [22]. The model is obtained from the high-Reynolds-number asymptotic theory by replacing the laminar viscosity in the boundary and mixing layers (collectively termed hereafter as the cyclic layer) with turbulent viscosity. As a result, turbulence needs to be modelled only in thin layers, which is easier than modelling turbulence in the entire recirculating flow. Another important advantage is faster numerical calculations, as compared to using a full Reynolds-averaged Navier–Stokes solver. Such an approach assumes that the effective Reynolds number, that is the Reynolds number based on turbulent viscosity, is high. This is not in general true for massively separated flows, since large-scale vortex shedding results in large Reynolds stresses. However, once large-scale vortex shedding is prevented either by stabilisation or by the geometry, one can hope that this approximate model will be suitable. Note also that the Prandtl-Batchelor theorem might not apply to mean turbulent flow even if the turbulent viscosity is small, since this theorem is proved for constant viscosity. These issues can only be resolved by comparisons with experiments, and such comparisons will be described later in the present paper. The justification for the

[2] The high-Reynolds number limit of a viscous flow is of course singular: inviscid flow is only one of the distinguished limits, and there are many other limits, most notably, the distinguished limit in which viscous flow tends to the boundary layer flow. For more detail see references [21–23].

high-Reynolds-number laminar asymptotics is given in [22]; here we simply explain the resulting approximate model.

The implied geometry is illustrated in Fig. 1(a): the flow approaches the vortex cell along the wall from left to right, separates from the cusp and then reattaches. The model has two coupled components: an inviscid Batchelor model flow [20] and the thin viscous layers. The inviscid model neglects the thickness of the boundary and mixing layers. The vorticity ω is zero outside the area of closed streamlines and is constant inside it. There is a discontinuous drop B in the total pressure across the dividing streamline. The stream function of this flow satisfies the equation

$$\nabla^2\Psi \;=\; -\omega(\Psi) + B\delta(\Psi), \quad \text{with} \quad \omega \;=\; \begin{cases} 0, & \Psi \geq 0 \\ \omega_0, & \Psi < 0 \end{cases} \tag{1}$$

where δ denotes the Dirac delta. Here, the Dirac delta should be understood as a limit of a non-negative function of Ψ with finite support as the size of the support tends to zero while the integral of this function over the support domain remains equal to unity. The stream function vanishes along the body boundaries. The separatrix is the curve where $\Psi = 0$, with $\Psi > 0$ outside and $\Psi < 0$ inside the vortex cell. At infinity the velocity tends to a given value. With these boundary conditions (1) has a two-parameter family of solutions depending on the constant vorticity ω_0 in the eddy and on the jump B in the total pressure across the mixing layer. Enforcing the Kutta–condition at the cusp A determines one of the parameters, say B for a fixed ω_0, but the other cannot be found within the framework of inviscid flow. Its value must be determined by the condition that the solution in the cyclic layer exists and matches the Batchelor model flow.

The second component of the model is the thin viscous layers. It consists of the oncoming and outgoing boundary layers upstream of the cusp A and downstream of the reattachment point B, the cyclic boundary layer including the mixing layer around the separatrix between A and B, and the boundary layer developing in the reversed flow along the vortex cell wall between B and A. In the boundary layers it is natural to use a coordinate system attached to the wall and/or separatrix with streamwise s and normal n coordinates. The oncoming boundary layer starts somewhere upstream (say, at the forward stagnation point in the case of a flow past a body) and ends at the cusp $s = 0$. The mixing layer is between $s = 0$ and $s = s_B$. The outgoing boundary layer is not considered in the present paper. The reversed flow boundary layer is between $s = s_B$ and $s = s_A$. Let p denote the static pressure and u the velocity component in the streamwise direction. It is convenient to use the von-Mises formulation, in which n is substituted by the stream function ψ under the transformation $(s, n) \rightleftarrows (s, \psi)$ via

$$\psi(s,n) \;=\; \int_0^n u(s,\tilde{n})\mathrm{d}\tilde{n}, \qquad \text{so that} \qquad n(s,\psi) \;=\; \int_0^{\psi} \frac{1}{u(s,\tilde{\psi})}\,\mathrm{d}\tilde{\psi} \tag{2}$$

as discussed in Schlichting [27]. With the introduction of so-called "total head" or total pressure

$$g(s,\psi) \;=\; \frac{u(s,\psi)^2}{2} + p(s) \tag{3}$$

the boundary layer equation reduces to

$$\frac{\partial g}{\partial s}(s,\psi) \;=\; u(s,\psi)\frac{\partial}{\partial \Psi}\left[\frac{1}{Re_{\mathrm{eff}}(s,\psi)}\cdot\frac{\partial g}{\partial \Psi}\,(s,\psi)\right]. \tag{4}$$

All the quantities here are assumed to be suitably non-dimensionalised. The effective Reynolds number $Re_{\mathrm{eff}} = (L_r u_r/(\nu + \nu_t)$ based on a characteristic reference velocity u_r and length scale L_r is a function of the so-called effective viscosity. The effective viscosity can be expressed as the sum of the molecular viscosity ν and a much larger artificial "eddy-viscosity" $\nu(s,\psi)$, which models the local effect of the Reynolds stresses on the turbulent mean flow through turbulence models. Obtaining g from (4) is equivalent to solving the full boundary layer equations, as one can readily recover u from

$$u(s,\psi) \;=\; \sqrt{2(g(s,\psi) - p(s))} \tag{5}$$

which allows the other velocity component to be determined by integration from the continuity equation.

In the same way as in the asymptotic theory [22], the regions near the points A and B are assumed to be effectively inviscid. This means that inside these regions the Bernoulli equation applies. As a result, inside these regions the total pressure g is constant along the streamlines. Therefore, one can calculate the oncoming boundary layer and then use the profile of g at the end of it (that is at point A at $s = 0$) as the initial profile for the upper part of the mixing layer. Equivalently, one can simply include the oncoming boundary layer into the cyclic layer domain. At the point B the mixing layer divides. Its upper part continues downstream as an outgoing boundary layer, while the lower part turns, giving rise to the boundary layer inside the vortex cell. The total pressure profile at the end of this layer serves as the initial profile in the lower part of the mixing layer. This is expressed by the condition

$$g(0,\psi) \;=\; g(s_A,\psi), \quad \psi < 0. \tag{6}$$

A resulting schematic of the flow is shown in Fig. 1(b). Assuming that the oncoming boundary layer starts at, say, $s = s_s$, one should impose also the initial condition

$$g(s_s,\psi) \;=\; g_s(\psi) \tag{7}$$

with $g_s(\psi)$ given. The solution of (4) is sought in the domain $\mathrm{I} + \mathrm{II} + \mathrm{III}$ in Fig. 1(b), that is in $\{s,\ \psi{:}s_s \leq s \leq 0,\ 0 \leq \psi \leq +\infty\} \cup \{s,\ \psi{:}0 \leq s \leq s_B,\ -\infty \leq \psi < +\infty\} \cup \{s,\ \psi{:}s_B \leq s \leq s_A,\ -\infty \leq \psi \leq 0\}$. The standard no-slip condition is imposed at the walls: $u_{|\mathrm{wall}} = 0$, or, equivalently,

$$g_{|\mathrm{wall}} \;=\; p(s). \tag{8}$$

The pressure distribution in the boundary layer is obtained from a so-called matching condition with the outer inviscid flow. Let $P(s, n)$ and $G(s, n)$ denote, respectively, the static and total pressures in the Batchelor model flow (1). Then

$$p(s) \;=\; P(s,0). \tag{9}$$

A matching condition should also be imposed on the velocity or, equivalently, on the total pressure. If the initial velocity profile in the oncoming boundary layer satisfies this condition, then the boundary layer solution will satisfy it automatically on the external side of the cyclic layer. However, there is no initial profile on its internal side. Noting that $G(s, n)$ is discontinuous across $n = 0$: $G(s, +0) - G(s, -0) = B$, the appropriate matching condition for the total pressure there is

$$\lim_{\psi \to -\infty} g(s,\psi) - G(s,-0) \;=\; 0. \tag{10}$$

Equations (1–10) give the full formulation of the problem to be solved. With the Kutta condition imposed this system can have a solution only for one value of ω_0, thus determining this value, because for an arbitrarily selected ω_0 the viscous part of the problem, that is (7–10), has no solution. It also has no solution if one of the boundary layers separates or the mixing layer breaks down under the action of an unfavourable pressure gradient.

Note the way the inviscid and viscous problems are coupled. The viscous part depends on the pressure distribution from the inviscid solution. The parameter ω_0 of the inviscid solution is determined from the solvability condition for the viscous part. The solvability condition is inconvenient for numerical calculations. One can replace (10) with a weaker condition $\partial g(s,\psi)/\partial\psi \to 0$ as $\psi \to -\infty$. Then the solution can be found for a given ω_0, so that $\lim_{\psi\to-\infty} g(s,\psi) - G(s,-0) = f(\omega_0)$, and then ω_0 can be found numerically by solving the equation $f(\omega_0)=0$.

This model gives two values at a point for every quantity. Say, the velocity and total pressure are given by $G(s, n)$ and by $g(s, n)$. These correspond to two different distinguished limits arising in the asymptotic prototype of the model. To obtain the final result one needs to build the composite expansion in the standard way [23]. For the total pressure inside the eddy, for example, it is given by

$$g = g(s,\psi) + G(s,n) - G(s,-0). \tag{11}$$

3. Finite-difference scheme and solution procedure

The overall approach to solving the boundary layer equations in von-Mises variables is the same as that used in [22] for purely laminar flow. Since more details can be found there only an outline to explain the inclusion of the turbulent Reynolds stresses is given here.

Algebraic grid-stretching in s and Ψ based on the arctan-function facilitates a concentration of grid points in regions with large gradients. While a second order discretisation in the wall-normal Ψ-direction is adopted throughout, a mixed scheme in s automatically adjusts its order to the local streamwise grid-density. The idea is to utilise second order s-discretisation wherever the grid is relatively coarse and higher accuracy is therefore needed, but a monotone first order scheme wherever the grid is locally fine enough that this robust scheme is affordable. That way the stability of the scheme can be improved without reducing the overall order of approximation.

To simplify the notation let $q_{i,j} = q(s_i, \Psi_j)$ for any flow quantity q, with the new abbreviations $q_j = q_{i,\,j}$ and $\tilde{q}_j = q_{i+1,j}$ denoting its value at the present streamwise s-station and the following downstream one, respectively. Values at the collocation points between the grid points may be obtained by averaging neighbouring values in the streamwise $q_{i+1/2,j} = 1/2(\tilde{q}_j + q_j)$ or wall-normal $q_{j+1/2} = 1/2(q_{j+1}+q_j)$ direction. Local step sizes $\Delta s_{j+1} = s_{i+1} - s_i$ and $\Delta\Psi_{j+1} = \Psi_{j+1} - \Psi_j$ may vary according to the grid function. Finally, let $\mu_{\text{eff}} = 1/Re_{\text{eff}}(s,\Psi)$ denote the ratio between the local viscous and inertia forces.

Now the key observation is that the standard first order finite-difference formula for the first derivative is second order on equidistant and stretched grids alike, if applied to the midpoint between two grid points:

$$\left.\frac{\partial g}{\partial\Psi}\right|_j = \frac{g_{j+\frac{1}{2}} - g_{j-\frac{1}{2}}}{\frac{1}{2}(\Delta\Psi_{j+1} + \Delta\Psi_j)} + \mathcal{O}\left(\left\{1/2(\Delta\Psi_{j+1} + \Delta\Psi_j)\right\}^2\right) \tag{12}$$

The first order scheme in s solves equation (4) in a fully implicit manner at the point $(i+1, j)$ by applying (12) to its left hand side, which yields

$$\frac{\tilde{g}_j - g_j}{\Delta s_i} = \tilde{u}_j\left\{\frac{1}{\frac{1}{2}(\Delta\psi_{j+1} + \Delta\psi_j)}\left[\widetilde{\mu}_{\text{eff}_{j+\frac{1}{2}}}\left(\frac{\tilde{g}_{j+1} - \tilde{g}_j}{\Delta\psi_{j+1}}\right) - \widetilde{\mu}_{\text{eff}_{j-\frac{1}{2}}}\left(\frac{\tilde{g}_j - \tilde{g}_{j-1}}{\Delta\psi_j}\right)\right]\right\} \tag{13}$$

For the second order scheme in s all parts of equation (4) are solved at the midpoint $(i+1/2+j)$. Values at the midpoint $s_{i+1/2+j}$ are obtained by averaging neighbouring points while the Ψ-derivative is treated as in (13):

$$\begin{aligned}\frac{\tilde{g}_j - g_j}{\Delta s_i} = u_{i+\frac{1}{2}j}\cdot\frac{1}{2}\Bigg\{&\frac{1}{\frac{1}{2}(\Delta\psi_{j+1} + \Delta\psi_j)}\left[\widetilde{\mu}_{\text{eff}_{j+\frac{1}{2}}}\left(\frac{\tilde{g}_{j+1} - \tilde{g}_j}{\Delta\psi_{j+1}}\right) - \widetilde{\mu}_{\text{eff}_{j-\frac{1}{2}}}\left(\frac{\tilde{g}_j - \tilde{g}_{j-1}}{\Delta\psi_j}\right)\right]\\ &+\frac{1}{\frac{1}{2}(\Delta\psi_{j+1} + \Delta\psi_j)}\left[\mu_{\text{eff}_{j+\frac{1}{2}}}\left(\frac{g_{j+1} - g_j}{\Delta\psi_{j+1}}\right) - \mu_{\text{eff}_{j-\frac{1}{2}}}\left(\frac{g_j - g_{j-1}}{\Delta\psi_j}\right)\right]\Bigg\}\end{aligned} \tag{14}$$

At every step in s simple iterations are performed for determining $\tilde{u}$ and $\widetilde{\mu}_{\text{eff}}$. Due to the parabolic nature of the transformed boundary layer equations (4) this approach results in a streamwise marching procedure, where the total pressure profile g at each new station is calculated implicitly. With three unknowns $\tilde{g}_{j+1}, \tilde{g}_j$ and $\tilde{g}_{j-1}$ per wall-normal grid point the discretisations (13) and (14) yield tridiagonal linear equation systems that can be solved efficiently with the Thomas algorithm.

Each simulation is started from an initial profile in the oncoming boundary layer. A single boundary layer calculation through subregion I in Fig. 1(b) provides the upper half of the initial condition for the mixing layer in the form of a cusp profile. The initial condition for the lower half of the g-profile is taken arbitrarily as piecewise polynomial of a suitable shape. Then a sequence of calculations in the sub-regions II and III is performed until convergence, with the use of (6) as indicated with a dashed line in Fig. 1(b). Additionally, an Aitken extrapolation of the g-profile at the end of each full vortex cell cycle is used to speed up this process. As in [22], condition (10) is imposed at a sufficiently large but finite negative value of $\psi = \psi_{-\infty}$. A secant method is then used to find the vorticity ω_0 such that $\partial g/\partial\psi = 0$ at a point on the boundary $\psi = \psi_{-\infty}$ of the computational domain. Note that the convergence of the cyclic iterations is due to the action of viscosity, and this has certain implications for the selection of the model of turbulence, see below.

The implementation of the scheme without turbulence models was verified against the exact solution [19] for the constant vorticity ω of the fluid in a cylinder, whose walls are partly in steady rotation and partly fixed. Within the vortex cell code the moving wall could be mimicked by a "mixing layer" of one grid point in the wall-normal direction, which moves with the prescribed wall velocity as an upper free stream velocity. Usual grid refinement and computational domain size sensitivity tests were made to ensure that numerical errors are less than the variance of the experimental results.

The simulations with the use of turbulence modelling also allow a qualitative comparison with the laminar flow field in an elongated vortex cell investigated by [22]. Fig. 2 exemplifies the development of turbulent boundary layer profiles within a vortex cell. (This corresponds to the flow in the experimental facility for $\phi = 40^\circ$ and $Re_d = 94{,}000$ described below, but these details are not essential for our illustration here.) At the cusp the inner boundary layer merges with the external oncoming boundary layer. The now separated flow develops into a mixing layer, which exhibits a shear layer profile with a pronounced velocity deficit near the dividing streamline, stemming from the presence of the wall in both streams upstream at the cusp. Further downstream this deficit is smoothed out to some extent under the influence of friction until the

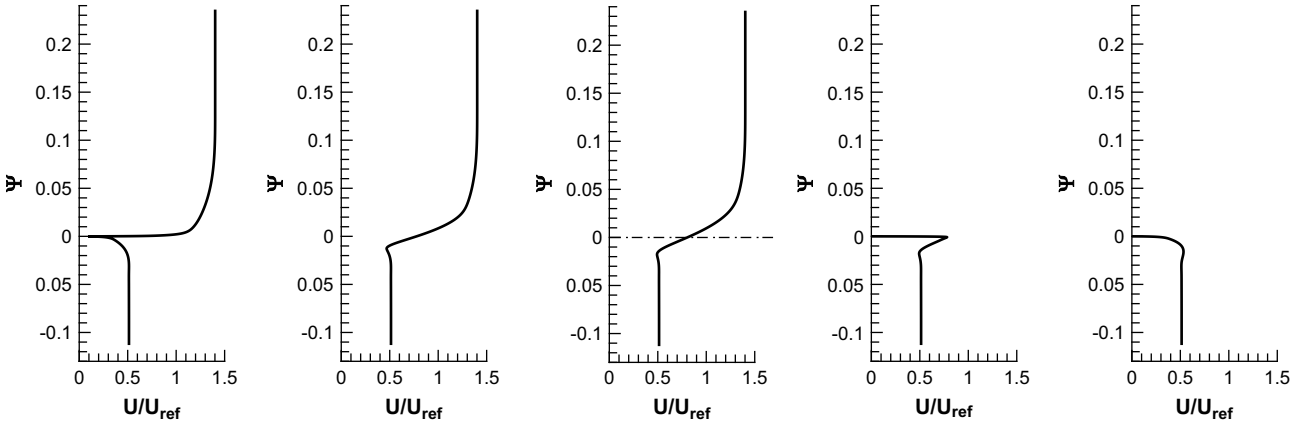

Fig. 2. Streamwise velocity as a function of ψ. From left to right: profile at cusp, middle of mixing layer, end of mixing layer, immediately after the reattachment point, and in the middle of the wall bounded section.

impinging shear layer divides into an inner and an outer flow at the stagnation point. Note that the velocity on the dividing streamline just before impingement is noticeably higher than the flow velocity at the edge of the boundary layer inside, as the local velocity minimum has moved downwards. This leads to a velocity excess in the near-wall region at the start of the wall bounded part of the cell. However, it is quickly smoothed out by the wall friction, so that an ordinary boundary profile redevelops before the cusp is encountered again.

All these features appear in the laminar flow field of the vortex cell in [22] (see Figs. 2 and 7 there), the only differences stemming from three tangential wall jets employed by Bunyakin et al. towards the end of the wall bounded part to avoid secondary separation.

4. Turbulence modelling

For the wall bounded parts of the geometry the two-layer models of Baldwin–Lomax [24] and Cebeci–Smith [25] were tested in several variants described in White [26] against measurements described in the following sections. For the mixing layer "free shear layer" models can be employed, the simplest of which dates back to Prandtl, who considered a zero pressure gradient shear layer between two streams with a higher velocity $u_{\max}$ at the top and a lower one $u_{\min}$ at the bottom [27] and wrote

$$\nu_t = \alpha \delta_{\text{mix}} (u_{\max} - u_{\min}) \tag{15}$$

This gives a constant eddy-viscosity distribution ν in the vertical direction with the eddy-viscosity assumed to be proportional to the product of the thickness δ_{mix} of the mixing layer

$$\delta_{\text{mix}} = y_{\text{up}} - y_{\text{down}}, \quad \text{with}$$

$$y_{\text{up}} = \left\{ y \in [y_{\min}, y_{\max}] \left| \frac{(u(y) - u_{\min})^2}{(u_{\max} - u_{\min})^2} = \frac{9}{10} \right. \right\} \tag{16}$$

$$y_{\text{down}} = \left\{ y \in [y_{\min}, y_{\max}] \left| \frac{(u(y) - u_{\min})^2}{(u_{\max} - u_{\min})^2} = \frac{1}{10} \right. \right\} \tag{17}$$

and the velocity difference across the shear layer. The only closure coefficient is the factor $\alpha = 0.014$ in (15), which gives excellent agreement to an experiment with $u_{\min} = 0$ (see Schlichting [27], Fig. 23.3). A slightly more advanced approach described by Wilcox [28], Section 3.3.2, utilises Prandtl's mixing length theory

$$\nu_t(y) = l_{\text{mix}}^2 \left| \frac{\partial u}{\partial y}(y) \right| \quad \text{using} \quad l_{\text{mix}} = \alpha \delta_{\text{mix}} \tag{18}$$

where δ_{mix} is defined as in (16); in this case the only closure coefficient is the factor $\alpha = 0.071$ in (18).

Best agreement for the wall bounded parts was obtained with the Baldwin–Lomax model subjected to the Cebeci–Smith pressure gradient correction

$$A^+ = A_o^+ \left[1 + y \frac{\partial P / \partial x}{\rho u_\tau^2} \right]^{-\frac{1}{2}} \quad \text{applied to} \quad l_{\text{mix}} = \kappa y \left[1 - e^{-y^+ / A^+} \right] \tag{19}$$

which adjusts the standard model parameter $A_o^+ = 26$ for the van Driest damping to changing pressure gradients. While Wilcox's model (18) was more accurate than Prandtl's (15) for the mixing layer, it causes significantly longer convergence times. This is especially true for vertically extended domains due to a quickly vanishing viscosity outside of the core region of the shear layer. The linear combination

$$\nu_t = C \nu_{t,\text{Prandtl}} + (1 - C) \nu_{t,\text{Wilcox}} \tag{20}$$

combines both advantages. A fine-tuning of C to 0.1 even resulted in a slightly better overall agreement compared to the original Wilcox-model. Thus, this model in connection with the Baldwin–Lomax model subject to (19) was used in the computations presented below.

5. The validation of the cyclic boundary layer code

5.1. Experimental realisation of a generic model vortex cell

The model we develop is intended for use with flows with trapped vortices, that is flows with closed streamline eddies but without large-scale vortex shedding. A special facility (Fig. 3) was built, the geometry of which ensures that no large-scale vortex shedding occurs even without active stabilisation measures (see [29] for more detail). It consists of a centrifugal fan, expansion section, a settling chamber and a two-dimensional contraction leading to a rectangular channel. The maximum main stream velocity U_{ref} in the channel section, which was monitored with a Pitot-static tube during all experiments, was 14 m/s. The cylindrical vortex cell is mounted at the bottom end of the rectangular channel section, with the flow guided around it by a larger cylinder section. Its spanwise dimension is 8.6 diameters. The key

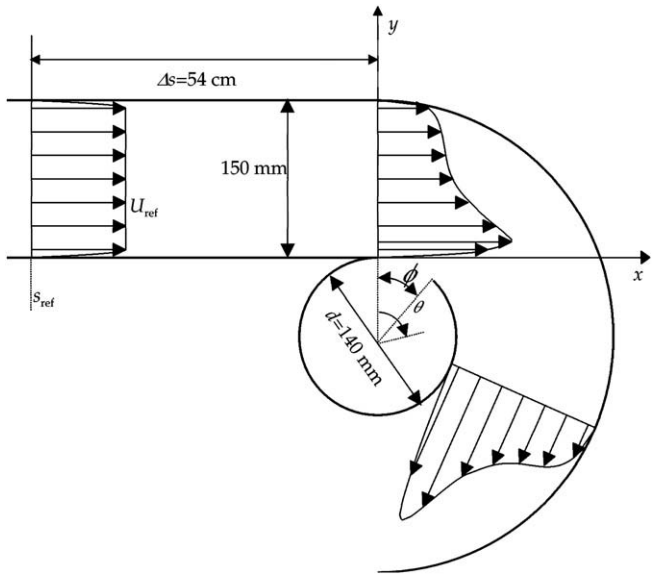

Fig. 3. Measurement section of the rig. The contraction exit is 1m upstream of the separation point ($\phi = 0°$), the so-called cusp.

parameter of a vortex cell, the length of its separatrix, was varied by adjusting the opening angle ϕ (see Fig. 3) between 20° and 120°. The plexi-glass construction of the set-up enabled the application of Laser-Doppler Anemometry (inside the cell), which comprised a two-component Dantec Fibreflow system using a Spectra Physics 5 W Argon-Ion laser.

Experiments were undertaken for Reynolds numbers $Re_d = 54{,}000$, 94,000 and 132,000 based on the velocity U_{ref} at the reference station s_{ref} depictured in Fig. 3, the inner vortex cell diameter $d = 0.14$ m and a dynamic viscosity of 14.6×10^{-6} m^2/s. Experimental results are available for the opening angles $\phi = 40°$ and 60° for all Reynolds numbers, with an additional measurement for a smaller opening angle of $\phi = 20°$ for $Re_d = 94{,}000$ only.

5.2. Rig calculations

To apply our model for a particular situation one needs to have a solution for the inviscid Batchelor model problem (1) and the initial velocity, or total pressure profile (7). In practice one needs also to know the state of the oncoming boundary layer, which was in fact laminar or transitional in the particular experiments in the rig.

The Batchelor model flow solution for the experimental facility was found approximately by assuming the separatrix to be a part of the same circle as the vortex cell. In this case the constant vorticity flow inside the cell is a simple solid-body rotation. Outside, the irrotational flow is found by means of a chain of conformal mappings inspired by the procedure suggested by Ives [30].[3] Note that, according to this solution, the flow accelerates along the wall while approaching the cusp, so that the oncoming boundary layer is under the action of a relatively strong favourable pressure gradient. The Bernoulli constant jump B is the only free parameter. Within our approximation its value affects only the flow inside the eddy. Hence, the oncoming boundary layer needs to be calculated only once for each value of Re_d. This gives the initial profile for the upper part of the mixing layer. In principle, one could use the velocity profiles measured above the cusp as the initial profiles for the mixing layer. However, calculating the oncoming boundary layer between the start section and the cusp gives additional information about the state of the boundary layer, as discussed below.

The initial velocity profiles were measured at the reference station s_{ref} of Fig. 3 which was nearly four times the cell diameter d upstream of the cusp, where the influence of variations in the opening angle ϕ was negligible. Accordingly, only the 40° – case was measured. Fig. 4(a) shows the measured velocity profiles and the best fits by laminar Blasius profile and by a turbulent 1/7-power-law profile. Blasius profiles fit the measurements for the two lower Reynolds numbers, but for the higher one neither fit is good. This confirms the experimental findings that the flow is laminar at s_{ref} for the two lower Reynolds numbers, while for the highest Reynolds number the flow is transitional at s_{ref}.

The further development of the oncoming flow is influenced by the flow acceleration upstream of the cusp induced by an upstream effect of the semi-circular end-section and the associated 1/radius distribution of the inviscid channel core velocity. Within this region the inviscid wall velocity increases by 40%. The inviscid flow solution for the oncoming flow is in a very good agreement with experimental data in the potential flow region, as demonstrated by Fig. 3 in Savelsberg & Castro [29]. The experiments also showed that the opening angle (for $\phi \in [20°; 60°]$) had very little effect on the profiles of the velocity above the cusp. The acceleration manifests itself by the deviation of these cusp profiles from the vertical channel flow profile, which can be seen above the boundary layer in Fig. 5. Low levels of turbulent shear stresses measured above the cusp indicate that even for the highest Reynolds number the flow has been relaminarised to some extent as a result of the favourable pressure gradient. However, all velocity measurements inside the vortex cell yielded turbulent fluctuations on the order of 10% relative to the upstream reference velocity. This confirms that regardless of the state of the oncoming boundary layer the separating shear layer is turbulent for all Re_d.

For many practical applications the oncoming boundary layer would be fully turbulent, but for the comparisons of the theoretical prediction with the experiment in the rig one has to guess the transition position where the turbulence model is switched on. This guess can be made on the basis of the comparison of the predicted and measured velocity profiles above the cusp. For the highest Reynolds number a fully turbulent calculation starting from the already transitional initial-condition-profile from Fig. 4(b) results in the outer cusp profile shown in Fig. 5(a). For the medium Reynolds number the laminar flow conditions from Fig. 4(a) at the reference station suggests that transition takes place between S_{ref} and the cusp. Best agreement with the measured cusp profile of Fig. 5(c) is obtained if the turbulence model is switched on after 15% of the total distance to the cusp. Finally, a fully laminar calculation for the lowest Reynolds number yields the cusp profile depictured in Fig. 5(e). The excellent agreement of the resulting cusp profiles with the experiment shows that the channel flow of the oncoming boundary for an opening angle of $\phi = 40°$ can be modelled to be laminar, transitional and turbulent for the Reynolds numbers $Re_d = 54{,}000$, 94,000, 132,000, respectively. For calculating the flow inside the cell these initial conditions and flow regimes were applied also to the other opening angles. This gave a comparable but in some cases slightly worse agreement with the respective measurements at the cusp.

5.3. Comparisons

We define rotational velocity u_{rot} as the velocity at the vortex cell walls and below the mixing layer for a solid-body rotation. For the cyclic boundary layer code u_{rot} can be readily calculated from the total pressure P_0^{in} of the converged solution and the constant

[3] The authors would like to express their gratitude to their project partner Prof. L. Zannetti from the Politecnico di Torino, who kindly provided this inviscid solution but thought it so simple as not to justify him becoming a co-author of this paper.

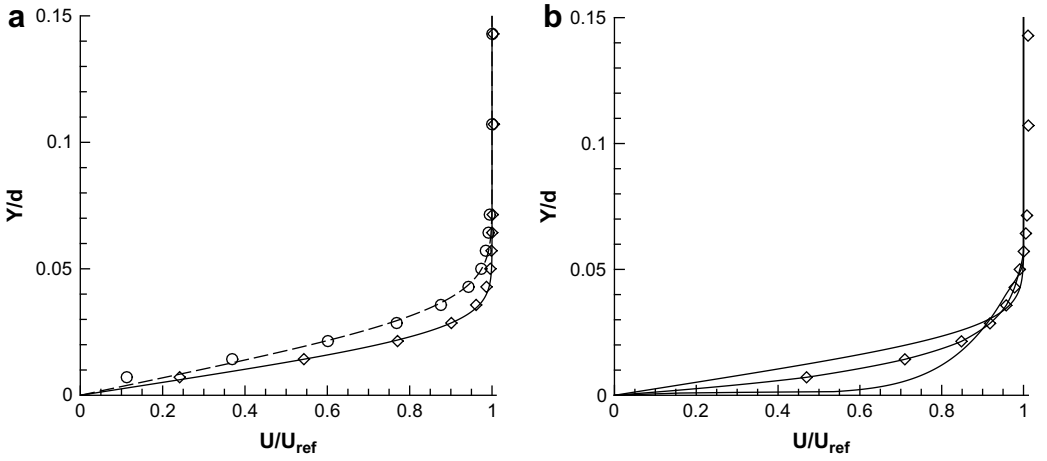

Best fit of Blasius profiles to measurements at $Re_d = 54,000$ *(dashed) and* $Re_d = 94,000$ *(line).*

Best fit by a Blasius-profile (dash-dotted) and a turbulent 1/7-power law profile (dashed) to experiments at $Re_d = 132,000$.

Fig. 4. Initial profiles at the reference station $s_{ref} \approx 4$ d upstream of the cusp. Lines: BL-code, symbols: LDA-measurements.

static pressure p inside the cell by invoking (5). Ideally, in order to obtain the rotational velocity u_{rot} from the experimental data, one would fit a straight line to the measured velocity profile through the core of the cell. Then the slope of the line is the angular velocity σ, and $u_{rot} = \sigma d/2$. However, despite the circular shape of the rig, the measured velocity profiles have an *S*-shape visible in Fig. 6 in the inviscid core outside of the near-wall region. For this reason σ was calculated by taking the average of the derivatives $\partial u/\partial y$ at each measurement point instead. Points in the boundary layer, identifiable by the large value of the second derivative $\partial^2 u/\partial y^2$, were excluded from this average.

We suspect that three-dimensional effects are responsible for the observed *S*-shape in the experiment. Indications come from additional experiments documented in [29] and from the recent three-dimensional *LES*-calculations by Hokpunna & Manhart [31] for a near-circular vortex cell. While infinite aspect ratio simulations (with periodic boundary conditions in the spanwise direction) result in essentially straight velocity profiles in the potential core regions outside the boundary layer [31], Hokpunna & Manhart [32] observed qualitatively an *S*-shape comparable to the current measurements in Fig. 6 for cases with side walls.

Note that the main vortices at the downstream end of rectangular cavities frequently display a similar behaviour. The reader might want to compare the simulations of a quadratic cavity without side walls of Shu, Wang & Chew [33] and of Ghia, Ghia & Shin [34], which both show extended, straight core regions, with the measurements of Grace, Dewar and Wroblewski [35] in a shallow, rectangular cavity, which yields a distinct *S*-shape.

This preliminary evidence suggests that this phenomenon is not restricted to circular vortex cells walls and should be taken into account for applications of cavities in general. Additionally, measurements in the cyclic rig show that while the mean rotational core velocity u_{rot} is fairly independent of the spanwise position, the spanwise velocity component w is non-zero and shows a roughly sinusoidal structure in span with peak velocities of up to 9% U_{ref} for the current width-to-cell diameter ratio of 8.6. Interestingly these large-scale oscillations with a spanwise wavelength of more than two d were absent for measurements in cells with aspect ratios of 2 and 5. Further data on these three-dimensional effects in cylindrical vortex cells with finite aspect ratio can be found in Savelsberg & Castro [29].

The right hand side of Fig. 5 shows the rotational velocity u_{rot} as a function of the opening angle for different values of the Reynolds number. Results from the cyclic boundary layer code are compared with the experimental data and a straightforward analytical estimate proposed by Savelsberg & Castro [29] in which the wall stress τ_w inside the vortex cell is approximated using a standard correlation for a planar turbulent boundary layer (see Schlichting [27]) and the shear stress in the mixing layer is modelled like in a planar mixing layer as $\tau_s \propto (u_c - u_{rot})^2$, where $u_c = 1.402 u_r$ is the inviscid wall velocity above the cusp, obtained from the inviscid solution of the external oncoming flow. The rotational velocity for a given opening angle ϕ then follows from the required balance between these stresses $(2\pi - \phi)\tau_w = \phi\tau_s$.

In both test cases for $Re_d = 132{,}000$ and the two higher opening angles $\phi = 40^\circ$ and 60° at $Re_d = 94{,}000$ the comparisons in Fig. 5 show good agreement between our cyclic boundary layer model, experiment, and the analytic estimate. For $\phi = 20^\circ$ at $Re_d = 94{,}000$ the cyclic boundary layer model still agrees well with the analytic estimate but the experimental value of u_{rot} is 9% lower. A smaller opening angle results in slower rotation inside the cell, which in turn may lead to thickening of wall boundary layer or to an increase in the relative importance of the 3D effects, thus explaining the observed deviation.

In the case of the lowest Reynolds number of $Re_d = 54{,}000$ experiments and the analytic estimate are in good agreement with each other, but the results of the cyclic layer model are about 13% lower, despite the obviously good agreement with the cusp profile demonstrated for the 40° – case in Fig. 5(e). However, the assumption of a fully turbulent oncoming boundary layer would lead to rotational velocities matching the results of the theory quite accurately (see triangles in Fig. 5(f)), although the cusp profile deviates noticeably from the measured profile as demonstrated for the 40° – case in Fig. 5(e). Note that although the laminar cusp profile in Fig. 5(e) exhibits higher velocities over the greater portion of the boundary layer, the resulting rotational speed is noticeably lower than for its turbulent counterpart. This is due to the structure of the turbulence models (18) and (15). In determining the value of the turbulent viscosity they rely on the boundary layer thickness, which is more than twice as large in the turbulent case, as demonstrated by the comparison with the corresponding inviscid velocity profile for the 40° – case in Fig. 5(e). Large turbulent viscosity increases the calculated friction in the mixing layer, thus driving a stronger rotation inside.

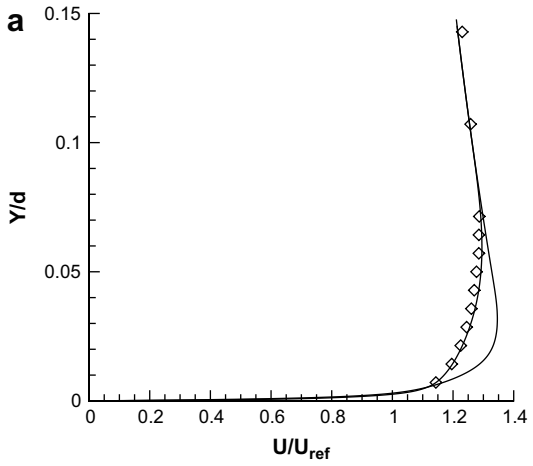

Comparison of cusp-profile at $Re_d = 132,000$.

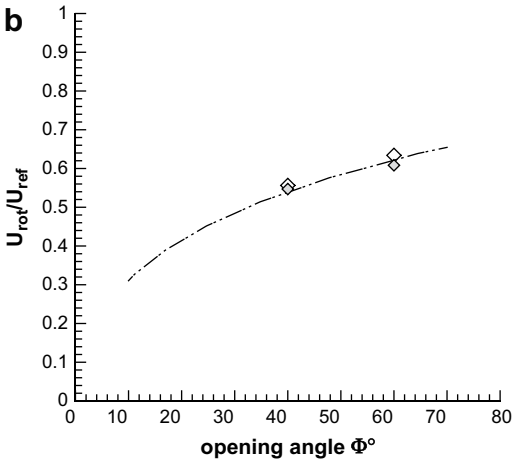

Comparison of u_{rot} *for* $Re_d = 132,000$.

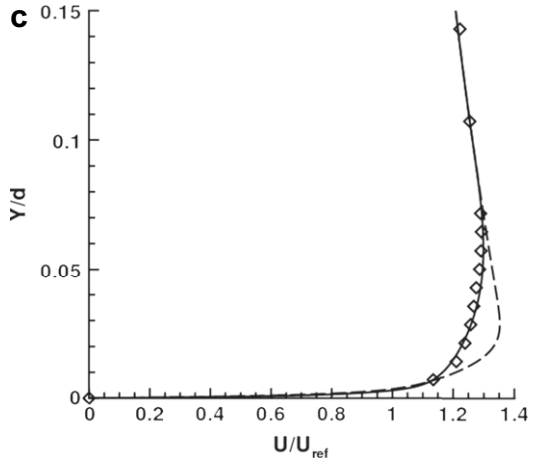

Comparison of cusp-profile at $Re_d = 94,000$.

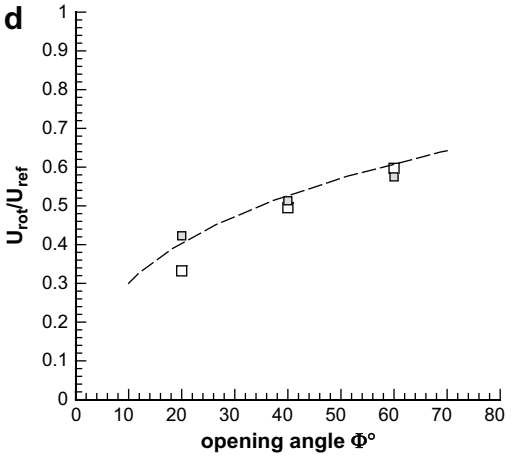

Comparison of u_{rot} *for* $Re_d = 94,000$.

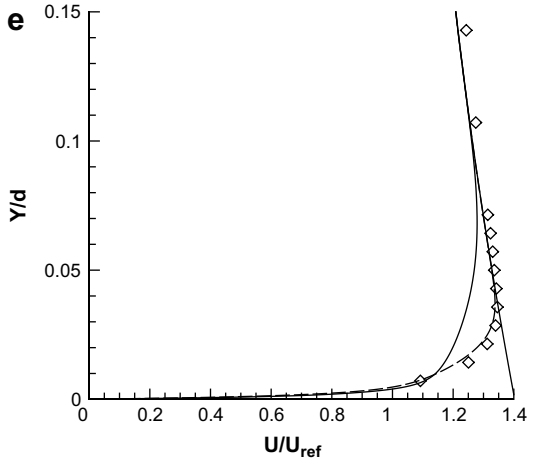

Comparison of cusp-profile at $Re_d = 54,000$.

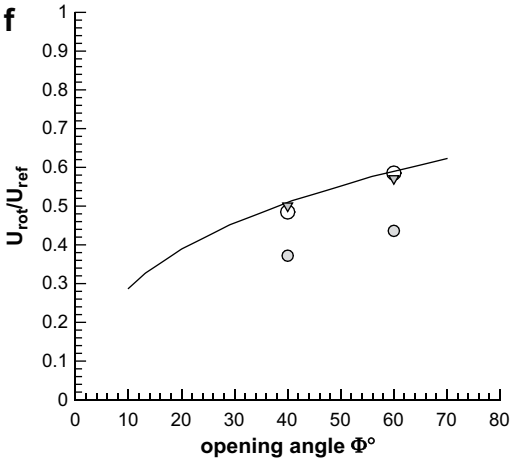

Comparison of u_{rot} *for* $Re_d = 54,000$.

Fig. 5. Left hand side: Comparison of the measured profiles (symbols) above the cusp for the $\phi = 40^\circ$ case against fully turbulent (line) and laminar (dashed) calculations of the oncoming boundary layer. Re = 94,000 only: line indicates result of modelling of transitional flow with turbulence model switched on at a position located 15% of the distance to the cusp after reference station S_{ref}. Additionally the inviscid profile is shown (dash-dotted). Right hand side: Comparison of the rotational velocity u_{rot} inside the vortex cell derived from experiment (open symbols), to simulations (filled symbols, calculations based on turbulent, transitional and laminar oncoming boundary layers from top to bottom) and a simple estimate [29] (lines). Re = 54,000 only: Additional triangles show simulation results, if the oncoming boundary layers are assumed to be turbulent.

Table 1 summarises the results of the comparisons. It shows that the model works only moderately well with errors in the order of 10–15% for vortex cells with short mixing layers, low Reynolds numbers and dominantly laminar or even relaminarised oncoming boundary layers, but very well with errors of only 2% for high Reynolds numbers, long mixing layers and turbulent oncoming boundary layers. It follows that the sophisticated transitional character of the oncoming boundary layer at the cusp, which is

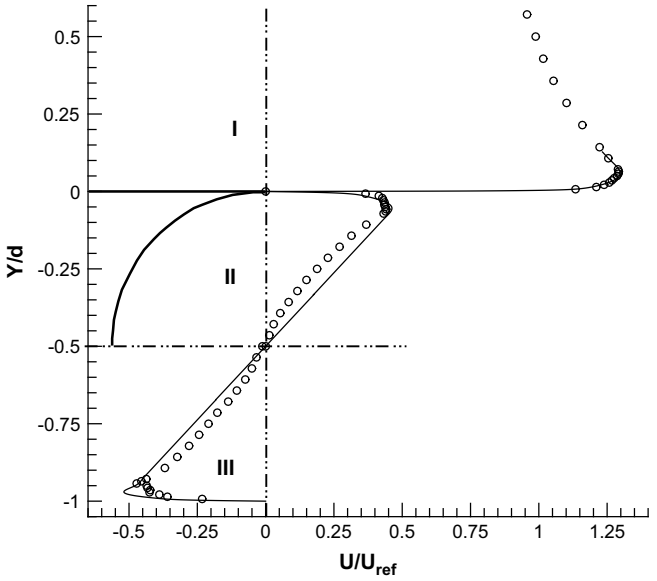

Fig. 6. Comparisons of the predicted (lines) and measured velocity profile for Re = 94,000 and opening angle of $\phi = 40°$. Note the S-shaped deviation of the measurements from the straight line in the eddy core.

under a relaminarising influence due to the outer flow acceleration but merges with a turbulent boundary layer from within the cell, is clearly beyond the scope of the algebraic turbulence models employed here, which implicitly assume a turbulent flow field in equilibrium. For dominantly turbulent flow fields, however, the model delivers convincing results. Finally, Fig. 6 shows the good agreement between the experimental measurements of the velocity profile and the prediction of the model obtained by composite expansion (11) for the $Re_d = 94{,}000$, $\phi = 40°$ case. Note, however, that the experimental points plotted were measured on the symmetry plane of the experimental rig. While the velocity profile in the core region is approximately spanwise-independent, in the boundary layer the velocity distribution shows significant three-dimensional effects.

6. Concluding remarks

According to our results, the fastest and the most accurate method of predicting the rotation speed inside the circular vortex cell similar to that in our experimental rig is the simple estimate of Savelsberg & Castro [29]. However, it is not clear how this estimate can be extended to non-circular cells where the pressure gradient is not zero. The cyclic layer model we proposed takes the pressure gradient into account quite naturally; however, we have only tested it for the case of zero pressure gradient. It appears to work well for higher Reynolds numbers but, perhaps not surprisingly, is less satisfactory when laminar-turbulent transition is involved. Unlike the model proposed here the estimate of [29] gives no means of determining the probability of any secondary separation – i.e. separation of the boundary layer on the wall of the cell – or the probability of a possible breakdown of the mixing layer under the action of an unfavourable pressure gradient. These effects, however, are likely to be the limiting factors in any attempt to optimise the performance of a vortex cell.

Importantly, the calculations with the present model are relatively fast. An alternative method would be to solve the Reynolds-averaged Navier–Stokes equations (RANS). We did compare our calculation times with calculations of a flow past a vortex cell made by our project partners at the Italian Aerospace Research Center (CIRA) using the commercial CFD package Fluent, and our

Table 1
Deviations of the cyclic boundary layer model result from experiment in percent of the respective reference velocity U_{ref}. Values in brackets for lowest Re_d are the results obtained assuming a fully turbulent oncoming boundary layer.

Re_d	U_{ref}, [m/s]	$\phi = 20°$, [%]	$\phi = 40°$, [%]	$\phi = 60°$, [%]
132,000	13.8	/	−2.2	−2.6
94,000	9.75	+9.1	+1.8	−0.9
54,000	5.6	/	−11.2 (3.4)	−15.9 (−2.4)

calculations are about two orders of magnitude faster. However, such a comparison does not take into account our use of an approximate analytic solution to (1). Therefore, one should expect that for a generic vortex cell shape the relative speed of calculations will be determined by the relative speed of solving (1) as compared to RANS. Naturally, (1) is much simpler to solve. While the method proposed in the present paper is faster, implementing it numerically is more complicated than using one of the many available RANS solvers but is particularly beneficial in situations when a large number of calculations is required, as, for example, in procedures of vortex cell shape optimisation. It should perhaps be emphasised that the techniques proposed here may not work as well for more general situations (and would certainly be difficult to implement in three-dimensional cases), but they are definitely appropriate for general cavity-type flows of the kind shown in Fig. 1.

Concerning the use of RANS, the results of the present study provide guidance on the selection of the turbulence model. Our results confirm that at least for vortex cells of near-circular shape it is sufficient to model the turbulent viscosity properly only in thin layers, while away from these, including within the vortex core, it is sufficient for the turbulence model to ensure that the flow is effectively inviscid. The restriction to near-circular cavities has to be made because if the geometry allows then solid-body rotation in the core will be the solution for any turbulence model, and it is the solid-body rotation which is given also by (1). Now, (1) is valid for high-Reynolds-number asymptotics of steady laminar flows, which implies small and constant viscosity. Turbulent viscosity inside the core of the vortex cell may also be small but it is likely to be not constant: therefore, the Prandtl-Batchelor theorem justifying the right hand side of (1) does not apply. However, from the practical viewpoint this restriction may be unimportant, since if the cell shape is far from circular there will be significant unfavourable pressure gradients, which are likely to cause secondary separation.

It can be concluded that the results obtained reveal certain physical features of flows in vortex cells and indicate that the proposed method of calculating such flows is useful.

Acknowledgements

The authors would like to thank Prof. L. Zannetti from the Politecnico di Torino, Prof. A. Iollo from the University of Bordeaux and Dr. E. Minisci from the University of Glasgow for stimulating discussions and Prof. Zannetti in particular for the inviscid flow solution utilised in the validation of the oncoming boundary layer. The financial support by the European Commission within its FP6 Programme, contract number AST4-CT-2005-012139 is gratefully acknowledged.

References

[1] F.O. Ringleb, Separation control by trapped vortices, in: G.V. Lachmann (Ed.), Boundary Layer and Flow Control, vol. I, Pergamon Press, London, 1961, pp. 265–294.
[2] E.J. Routh, Some applications of conjugate functions, Proc. London Math. Soc. 12 (1881) 73.
[3] M.I. Gurevich, On an error of F.O. Ringleb, Izv. AN SSSR, Mekhanika 1 (1967) 205–206 (in Russian).

[4] W.A. Kasper. 1974. Aircraft wing with vortex generation. United States Patent No. 3831885, Aug. 27, 1974.
[5] E.W. Kruppa. A Wind Tunnel Investigation of the Kasper Vortex Concept, AIAA-paper 77-310, 13th Annual meeting, Washington, D.C., January 10–13, 1977.
[6] J.M. Wu, J.Z. Wu, Vortex lift at a very high angle of attack with massively separated unsteady flow, in: R. Kawamura, Y. Aihara (Eds.), Fluid Dynamics of High Angle of Attack, Springer, 1993, pp. 35–63.
[7] S.I. Chernyshenko, Stabilization of trapped vortices by alternating blowing-suction, Phys. Fluids 7 (4) (1995) 802–807.
[8] http://www.ekip-aviation-concern.com/eng-b/4.shtml, (accessed 10.08.08).
[9] A.I. Savitsky, L.N. Schukin, V.G. Karelin, et al. 1995. Method for control of the boundary layer on the aerodynamic surface of an aircraft, and the aircraft provided with the boundary layer control system. United States Patent No. 5417391, May 23, 1995. (Preceded by earlier Russian patent No. 2015941 from 1991.)
[10] K. Koenig, A. Roshko, An experimental study of geometrical effects on the drag and flow field of two bluff bodies separated by a gap, J. Fluid Mech. 156 (1985) 167–204.
[11] P.A. Baranov, S.V. Guvernyuk, M.A. Zubin, S.A. Isaev, Numerical and physical modelling of the circulation flow in a vortex cell in the wall of a rectilinear channel, Fluid Dynamics 35 (5) (2000) 663–673.
[12] S.A. Isaev, S.V. Guvernyuk, M.A. Zubin, Y.S. Prigorodov, Numerical and physical modelling of a low-velocity air flow in a channel with a circular vortex cell, J. Eng. Thermophys. 73 (2) (2000) 337–344.
[13] T.W. Riddle, A.J. Wadcock, J. Tso, R.M. Cummings, An experimental analysis of vortex trapping techniques, J. Fluids Eng. 121 (3) (1999) 555–559.
[14] J.-Z. Wu, X.-Y. Luy, A.G. Denniz, M. Fan, J.-M. Wu, Post-stall flow control on an airfoil by local unsteady forcing, J. Fluid Mech. 371 (1998) 21–58.
[15] L. Cattafesta, D.R. Williams, C.W. Rowley, & F. Alvi. 2003. Review of active control of flow-induced cavity resonance. AIAA Paper 2003–3567.
[16] M. Pastoor, L. Henning, B.R. Noack, R. King, G. Tadmor, Feedback shear layer control for bluff body drag reduction, J. Fluid Mech. 608 (2008) 161–196.
[17] L. Zannetti, Vortex equilibrium in flows past bluff bodies, J. Fluid Mech. 562 (2006) 151–171.
[18] O.A. Ladyzhenskaya, The Mathematical Theory of Viscous Incompressible Flow, Gosudarstv. Izdat. Fiz.-Mat. Lit., Moscow, 1961, (In Russian. Engl. trans., New York-London-Paris: Gordon and Breach, Science Publishers, 1969.).
[19] G.K. Batchelor, On steady laminar flow with closed streamlines at large Reynolds number, J. Fluid Mech. 1 (1956) 177–190.
[20] G.K. Batchelor, A proposal concerning laminar wakes behind bluff bodies at large Reynolds number, J. Fluid Mech. 1 (1956) 388–398.
[21] S.I. Chernyshenko, Asymptotic theory of global separation, Appl. Mech. Rev. 51 (9) (1998) 523–536.
[22] A.V. Bunyakin, S.I. Chernyshenko, G.Y. Stepanov, High-Reynolds-number Batchelor-model asymptotics of a flow past an aerofoil with a vortex trapped in a cavity, J. Fluid Mech. 358 (1998) 238–297.
[23] J.D. Kevorkian, J.D. Cole, Perturbation Methods in Applied Mathematics, Springer-Verlag, New York, 1981, ISBN 0-387-90507-3.
[24] B.S. Baldwin, H. Lomax. 1978. Thin Layer Approximation and Algebraic Model for Separated Turbulent Flow. AIAA Paper 78–257.
[25] T. Cebeci, A.M.O. Smith, Analysis of Turbulent Boundary Layers, Academic, New York, 1974.
[26] F.M. White, Viscous Fluid Flow, Second ed. McGraw-Hill, 1991.
[27] H. Schlichting, Boundary Layer Theory, Fourth ed. McGraw-Hill, 1960.
[28] D.C. Wilcox, Turbulence Modeling for CFD, Second ed. DCW Industries, 1998, ISBN 0-9636051-5-1.
[29] R. Savelsberg, I.P. Castro, 'Vortex' flow in open cylindrical-section cavities, Exp. Fluid. (2008). doi:10.1007/s00348-008-0575-4.
[30] D.C. Ives, A modern look at conformal mappings, including multiply connected regions, AIAA J 14 (1976) 10061011.
[31] A. Hokpunna, M. Manhart, A large-eddy simulation of vortex cell flow with incoming turbulent boundary layer, Int. J. Mech. Syst. Sci. Eng. 1 (3) (2007) 123–128.
[32] Manhart, M. Head of Chair and Laboratory for Hydromechanics, Technical University of Munich, private communication.
[33] C. Shu, L. Wang, Y.T. Chew, Numerical computation of three-dimensional incompressible Navier–Stokes equations in primitive variable form by DQ method, Int. J. Numer. Meth. Fluid. 43 (2003) 345–368.
[34] U. Ghia, K.N. Ghia, C.T. Shin, High-Re solutions for incompressible flow using the Navier–Stokes equations and a multi-grid method, J. Comp. Phys. 48 (1982) 387–411.
[35] S.M. Grace, W.G. Dewar, D.E. Wroblewski, Experimental investigation of the flow characteristics within a shallow wall cavity for both laminar and turbulent upstream boundary layers, Exp. Fluid. 36 (2004) 791–804.